Quantum phase transitions in a $\nu = \frac{1}{2}$ bosonic fractional Chern insulator

Wei-Wei Luo,[1] Ai-Lei He,[1,2] Yuan Zhou,[1,3,*] Yi-Fei Wang,[4] and Chang-De Gong[1,3,4]

[1]*National Laboratory of Solid State Microstructures and Department of Physics, Nanjing University, Nanjing 210093, China*

[2]*Institute for Advanced Study, Tsinghua University, Beijing 100084, China*

[3]*Collaborative Innovation Center of Advanced Microstructures, Nanjing University, Nanjing 210093, China*

[4]*Center for Statistical and Theoretical Condensed Matter Physics, and Department of Physics, Zhejiang Normal University, Jinhua 321004, China*

(Received 24 April 2020; revised 18 September 2020; accepted 30 September 2020; published 15 October 2020)

Interacting quantum many-body systems often generate exotic orders, either topological or conventional competing orders. Understanding these phases and the phase transitions between them are common issues in condensed-matter physics. How to characterize these states in a convincing and convenient way remains ambiguous. Here, we report our numerical study on the interacting $\nu = \frac{1}{2}$ hard-core boson system with topological flat bands based on the infinite density matrix group algorithm. We explicitly show that the entanglement spectral flow can be used to diagnose the quantum phases emerging in the hard-core boson systems. In particular, the subsequent charge pumping exhibits a linear, sinelike, and indiscernible dependence by the flux threading in the fractional Chern insulator, supersolid, and solid state, respectively. The real-space boson occupancy in the thermodynamic limit is further calculated for a better understanding of the respective state. We compare the phase diagram obtained here with that obtained by the previously exact diagonalization method, and qualitative differences are observed. Therefore, the infinite density matrix group algorithm provides a convincing and convenient way to study the phase transition in such a strongly correlated topological system.

DOI: 10.1103/PhysRevB.102.155120

I. INTRODUCTION

Understanding strongly correlated systems is extremely challenging in condensed-matter physics. Exotic states have been theoretically predicted or experimentally observed, accompanied by the development of a variety of concepts and numerical methods. Conventionally, the phases can be classified by the concept of symmetry breaking proposed by Landau. High-temperature superconductivity in cuprates is one of the most famous symmetry-breaking states. The competition and coexistence of superconductivity and multiple competing orders, such as charge order, spin-density wave, and even other exotic orders, renders the pairing mechanism still controversial [1]. The emergence of the quantum Hall state [2] opens a new paradigm to characterize and classify phases of matter by topological order [3]. The precise quantization of the Hall conductance of two-dimensional electron gas at low temperature in a strong magnetic field, irrespective of the material details and local disorders, is well characterized by the topological invariants [4,5]. The fractional quantum Hall state [6,7] is also a topologically ordered state but with strong interactions. The usual fractional quantum Hall state requires the Landau level, a topologically nontrivial flat band realized in a strong magnetic field. Because of its theoretical importance and promising future applications, great interest and efforts have been devoted to realizing such an exotic phase in a much broader context. Following the pioneering work on the quantum anomalous Hall state or the Chern insulator state proposed by Haldane, where the integer quantum Hall state without the Landau level is realized on the honeycomb lattice with staggered flux threading [8,9], the fractional Chern insulator (FCI) is further proposed. The FCI, a highly correlated state analogous to the fractional quantum Hall state in a continuum, requires the dominant effect of interaction over kinetic energy and a topological band—a nearly flat band with nonzero Chern number. Three groups independently proposed candidate lattice models to produce the topological flat band (TFB) on kagome [10], honeycomb [11], and checkerboard lattices [11,12] by introducing the staggered fluxes or spin-orbit interactions together with the long-range hopping term in 2011. Since then, extensive works [13–15] have been carried out to search for the FCI state in the TFB system. Both the Abelian [16–18] and non-Abelian [19–21] FCI are established in the fermionic and bosonic systems. Several experimental schemes to realize the FCI in cold-atom systems [22–24] have also been proposed.

On the other hand, strong correlations also trigger a variety of electronic ordered states by symmetry breaking. The topological state, therefore, is challenged by other competing orders. Whether the topological state is robust against the quantum fluctuations remains unclear. Moreover, understanding the phases neighboring the FCI and their phase transitions can be a clue to search the FCI state in real materials. Theoretically, the convincing and convenient way to diagnose quantum phases is highly expected. The mean-field phase is often destroyed by quantum fluctuations. For example, the Chern insulating state predicted by mean-field studies [25–28] on a honeycomb lattice in the presence of short-range repulsive interactions was later shown to be complex charge

*zhouyuan@nju.edu.cn

or bond orders by more rigorous numerical methods [29,30]. The exact diagonalization (ED) method provides an unbiased evaluation of the model system; however, the resultant phases may be controversial due to the strong finite-size effect, especially in the ordered states [22]. In comparison, the infinite density matrix renormalization group (iDMRG) algorithm allows us to handle a larger system size and provides direct access to the spontaneous symmetry-breaking states in the thermodynamic limit [31]. Topological entanglement entropy and charge pumping have been proposed to identify the FCI nature [32–34]. However, a precise and straightforward way to characterize other competing ordered states is still elusive.

In this paper, we revisit the quantum phases and their transitions in the interacting $\nu = \frac{1}{2}$ hard-core bosonic TFB systems in two typical lattice models. Our purposes are twofold—compariing our diagnosis of the quantum phases obtained by the iDMRG algorithm with that obtained by the previous ED method [17], and more importantly finding the convincing and convenient way to characterize the quantum phase in a bosonic system. We show that the interaction-driven phase transition can be determined by the evolutions of some characteristic quantities. More importantly, we demonstrate unambiguously that the distinct phases in hard-core bosonic systems can be well diagnosed by the entanglement spectral flows and the resultant charge pumping features. In particular, we observe a linear dependence with $\frac{1}{2}$ charge-transferring, sinelike oscillation, and an insensitive response in the charge pumping with a quantum flux insertion in the FCI, the supersolid, and the solid state, respectively. The real-space boson occupancy patterns in various phases are further shown for direct visualizations. A comparison with the previous quantum phase obtained by the ED algorithm shows that the iDMRG algorithm offers a convincing and convenient way to identify the quantum phases in strongly correlated bosonic systems.

II. MODEL AND METHOD

We study the interacting hard-core bosons on two typical TFB lattice models, i.e., the extended version of the well-known Haldane model on the honeycomb lattice [35] and the checkerboard lattice [12]. The noninteracting Hamiltonian is written as

$$H = -t_1 \sum_{\langle ij\rangle} (e^{i\phi_1} b_i^\dagger b_j + \text{H.c.}) - \mathrm{t}_2 \sum_{\langle\langle \mathrm{ij}\rangle\rangle} (\mathrm{e}^{\mathrm{i}\phi_2} \mathrm{b}_\mathrm{i}^\dagger \mathrm{b}_\mathrm{j} + \text{H.c.}) - t_3 \sum_{\langle\langle\langle ij\rangle\rangle\rangle} (b_i^\dagger b_j + \text{H.c.}), \quad (1)$$

where $b_i^\dagger$ (b_i) creates (annihilates) a hard-core boson at the ith site. To generate the topological flat bands, the hopping terms up to the third-nearest-neighbor (NN) and an additional phase factor ϕ_2 in the second-NN (honeycomb) or ϕ_1 (checkerboard) in the NN hopping processes are included, as shown in Fig. 1. The optimal flatness ratio f is about 50 for the honeycomb lattice model with parameters $(t_1, t_2, t_3, \phi_1, \phi_2) = (1, 0.60, -0.58, 0, 0.4\pi)$, and about 30 for the checkerboard lattice model with $(t_1, t_2, t_3, \phi_1, \phi_2) = (-1, 1/(2+\sqrt{2}), -1/(2+2\sqrt{2}), 0.25\pi, 0)$ [12,17], and it will be adopted hereafter. To study the competition between the FCI and the other ordered states, we introduce the short-range repulsive interactions between the hard-core bosons expressed as

$$H_I = V_1 \sum_{\langle ij\rangle} n_i n_j + V_2 \sum_{\langle\langle ij\rangle\rangle} n_i n_j. \quad (2)$$

Here, $n_i = b_i^\dagger b_i$ is the number operator of bosons, and V_1 and V_2 denote the NN and second-NN repulsion strength between bosons, respectively. Recall that the bosonic systems discussed in this paper remain strongly correlated even in the absence of short-range repulsion due to the hard-core constraints. The above lattice models were previously studied using the ED algorithm [17].

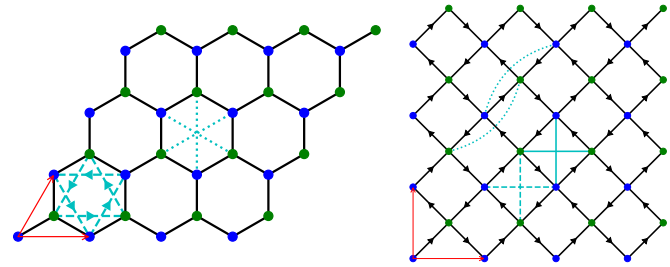

FIG. 1. Two typical lattice models harboring a topological flat band, where two red arrows in each lattice denote primitive lattice vectors. (a) The Haldane model on the honeycomb lattice. Solid, dashed, and dotted lines are the NN, second-NN, and third-NN hopping processes, respectively. Additional phase factors in the second-NN hopping process are denoted by arrows. (b) The checkerboard lattice model. Additional phase factors in the NN hopping processes are denoted by arrows. The cyan lines mark the second-NN hopping process, with solid and dashed lines for positive and negative t_1, respectively. The dotted lines depict the third-NN hopping process. The $(2 \times 4 \times 4)$-site lattice structures are chosen as typical MPS unit cells used in iDMRG calculations, although other unit cells are also studied.

We study the ground states of two lattice models by employing the iDMRG algorithm on an $L_x \times L_y$ cylinder, with L_x the length and L_y the circumference of the cylinder. In the iDMRG algorithm, a generic quantum state is compactly represented by the products of the matrices, hence the name matrix product state (MPS). For a local gapped Hamiltonian, the entanglement of the ground state usually obeys the area law. This allows us to faithfully represent such a ground state with a fairly small bond dimension χ, the maximum allowed matrix dimension in a MPS. In the same spirit, the Hamiltonian can also be written as a matrix product operator (MPO), which is sandwiched between two identical copies of the same MPS to express the energy expectation value as a tensor network. The ground state is thus obtained by iteratively optimizing each part of the MPS in this tensor network using the iDMRG algorithm. Typically, we can choose an MPS unit cell [36], which should be compatible with the translational symmetry of a represented state, with L_y lattice unit cells around the cylinder. Previous work on the iDMRG revealed that the FCI state can be identified by topological entanglement entropy [32,33] and a modular matrix [3,36,37]. The momentum-resolved entanglement spectrum [34] reveals the characteristic structure of edge modes. Hall conductance can be obtained by inserting the flux into the cylinder [38–43]. To

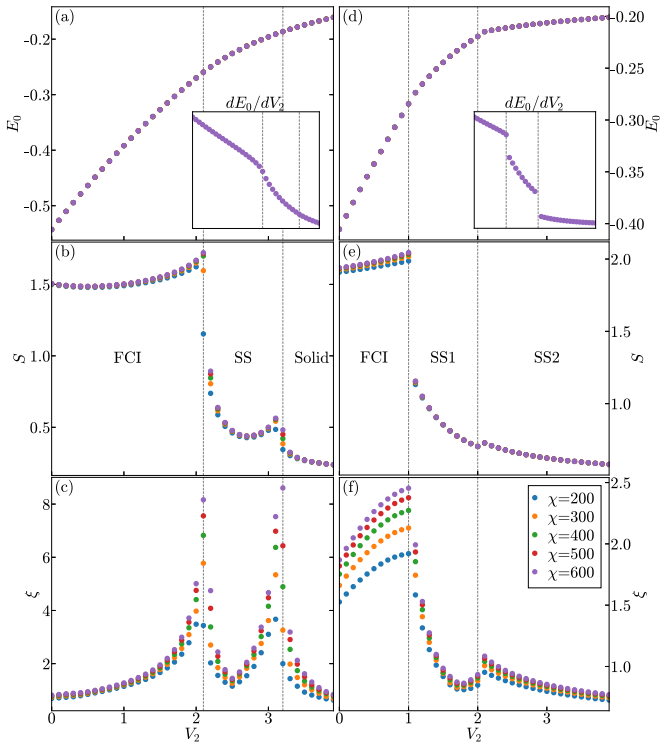

FIG. 2. Evolution of three characteristic quantities on the second-NN interaction V_2 with fixed $V_1 = 4$ in both the honeycomb (upper panels) and the checkerboard (lower panels) lattice model. (a),(d) Ground-state energy E_0, with the first derivative of the ground-state energy dE_0/dV_2; (b),(e) the entanglement entropy S; and (c),(f) the correlation length ξ. The iDMRG calculations are performed on an infinite cylinder of a $(2 \times 4 \times 4)$-site MPS unit cell with different bond dimensions χ labeled by colors. The notations for the respective phases in the middle panels will be discussed later.

accommodate the potentially translational symmetry-breaking states, which enlarge the lattice unit cell, we choose $4 \times L_y$ lattice unit cells instead, i.e., an MPS unit cell with $8L_y$ lattice sites. Several different sizes of L_y are attempted, and similar results are observed.

III. QUANTUM PHASES AND TRANSITIONS IN THE TFB LATTICE MODEL

We study the quantum phases and their transitions in the two bosonic models by using the iDMRG algorithm, and we compare them with the previous ED study [17]. We will focus more on the phase transitions and how to characterize the distinct quantum phases by the iDMRG method.

A. Honeycomb lattice model

We study the evolution of three quantities, i.e., the ground-state energy E_0, the entanglement entropy S, and the correlation length ξ, in order to analyze the candidate phases and phase transitions. In the honeycomb lattice model, three distinct phases can be well observed from the dependence of these quantities on the next-nearest-neighboring repulsion V_2 with the fixed nearest-neighboring repulsion $V_1 = 4$ as shown in the upper panels of Fig. 2. The continuity in the first-order derivative of the ground-state energy dE_0/dV_2 and the entanglement entropy, together with the lambda-like peaks in the correlation length ξ, strongly suggest the second-order phase transition occurred at $V_2 \sim 2.1$ and 3.2, respectively.

To diagnose these phases, we study the spectral flow ϵ in the entanglement spectrum by adiabatically inserting flux through the cylinder. The entanglement spectrum, obtained by cutting the infinite cylinder into two halves, faithfully captures the low-energy physics of edge modes [34]. For the weak second-NN repulsion V_2 (<2.1), a set of interpolating entanglement states flows across the gap. This process resembles the gapless edge modes on the boundary of the chiral topological insulators [44], manifesting the nontrivial topology of this phase. The entanglement spectrum can be further resolved by charge sectors Q_L (Fig. 3), which labels the $U(1)$ charges of the left Schmidt states [38,42]. In the absence of flux, the spectrum are exactly degenerate between the sectors $Q_L = \pm n$, with n an integer (only $n = 0$ and 1 are shown), yielding the charge polarization $\langle Q_L \rangle = 0$ on the left side of the cylinder. The degeneracy shifts to between the sectors $Q_L = -\frac{1}{2} \pm \frac{n}{2}$ with odd n after a flux quanta insertion, which results in the $-\frac{1}{2}$ fractional charge accumulation on the left side. Therefore, the exact $\frac{1}{2}$ charge pumping by a flux quanta insertion is observed [Fig. 3(d)]. Furthermore, the nearly linear evolution of $\langle Q_L \rangle$ on the inserting flux is also similar to that in the fermionic and bosonic FCI states [38,42]. These features provide convincing evidence that the present state is a FCI state. The FCI nature can be further supported by the fingerprint signature of the degeneracy sequence in the edge excitations. Due to the translational symmetry preservation in the y direction, each state in the entanglement spectrum can be labeled by the quantum number k_y. The first quasidegenerate sequence of six in the low-lying entanglement spectrum is $\{1, 1, 2, 3, 5, 7\}$ (Fig. 6), agreeing with the prediction of chiral Luttinger liquid theory for a Laughlin-like fractional quantum Hall state [44]. The FCI reported here is much robust against V_2 than that revealed by the ED algorithm [17], where the critical value of $V_2 \sim 1.0$. This may suggest that the strong quantum fluctuations will destroy the FCI state since they are overestimated in size.

In contrast, a large gap between the lowest entanglement level and the higher levels is found in the stronger $V_2 > 3.2$ cases. The entanglement spectrum does not respond to the threading flux, exhibiting the characteristic behavior of the conventional insulators. Consequently, the insensitive response of the charge pumping on the threading flux is observed [Fig. 3(d)]. These features demonstrate unambiguously that the present state is a solid state. In the intermediate interaction region of $2.1 < V_2 < 3.2$, a similar large gap exists in the entanglement spectral flow, suggesting a solidlike feature. However, a weak but visible sinelike feature is observed in the charge pumping [orange line in Fig. 3(d)], suggesting a metal-like feature. This feature is robust against the selected parameters, although the amplitude of oscillations decreases with increasing V_2, manifesting its universality in this state. Similar oscillations with flux insertion were observed in the Berry phase in the Fermi-liquid phase, although with a dominating linear dependence [16], signaling a metallic nature. Considering the bosonic nature, the weak metallicity in the

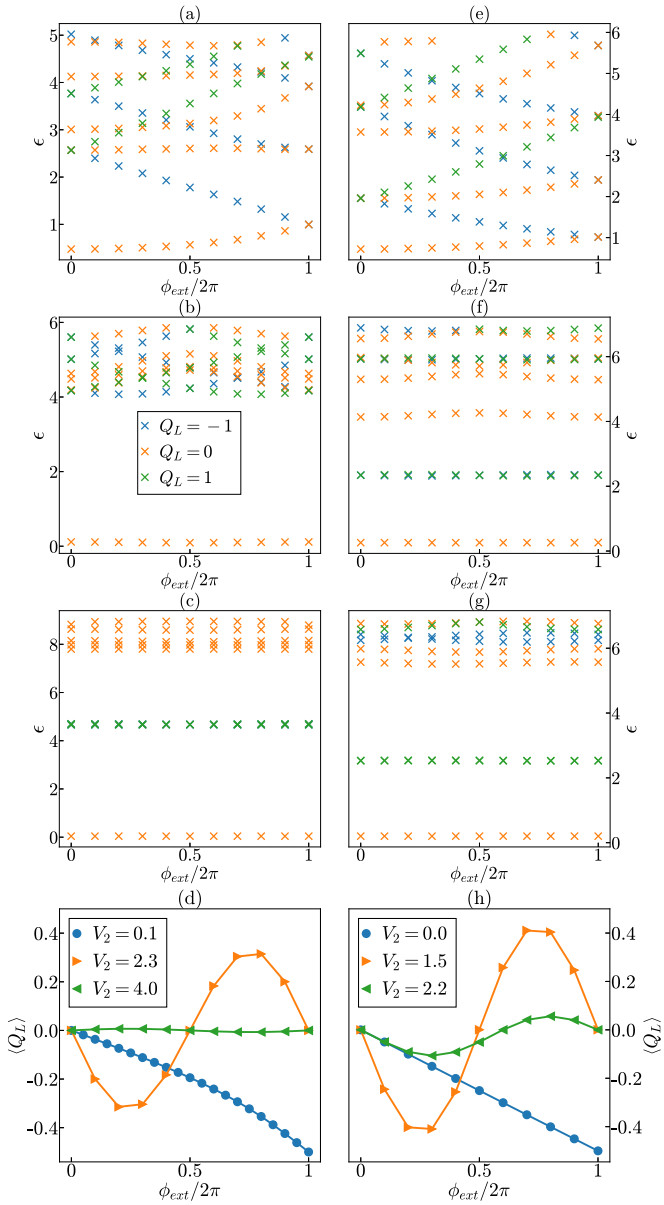

FIG. 3. Entanglement spectral flows with flux threading in different phases demonstrated in the text. Left panels are for the honeycomb lattice model with fixed $V_1 = 4$. (a) The FCI phase at $V_2 = 0.1$, (b) the supersolid state at $V_2 = 2.3$, and (c) the solid state at $V_2 = 4$. Right panels are for the checkerboard lattice model. (e) The FCI phase at $V_1 = 0, V_2 = 0$, (f) the supersolid-I phase at $V_1 = 4, V_2 = 1.5$, and (g) the supersolid-II phase at $V_1 = 4, V_2 = 2.2$. Different charge sectors with $Q_L = 0$ and ± 1 in the entanglement spectrum are coded by color. The lower panels (d) and (h) are the charge pumping at respective phases for the honeycomb and the checkerboard lattice models. The amplitude of $100 \times \langle Q_L \rangle$ in the supersolid and the solid state has been adopted to highlight the sinelike oscillations.

fermionic state is believed to be associated with the weak superfluid in the bosonic model. In fact, the V_2 dependence of the amplitude of sinelike oscillation agrees qualitatively with that of the superfluid density (not shown). The superfluid density is strongest near the phase boundary between the FCI and the supersolid state, and it decreases with increasing V_2. It

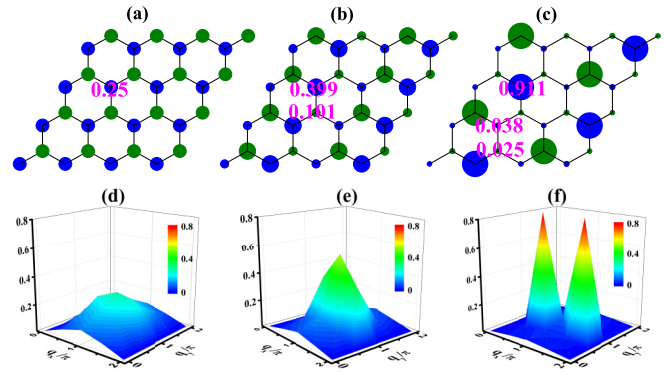

FIG. 4. Charge density profiles (upper panels) and corresponding structure factors (lower panels) of ground states in different phases in the honeycomb lattice model with fixed $V_1 = 4$. Parts (a) and (d) are for the FCI state at $V_2 = 0.1$ with homogeneous distributions, (b) and (e) are for the supersolid state at $V_2 = 2.3$ with stripy distributions, and (c) and (f) are for the solid state at $V_2 = 4$. The expectation value $\langle n_i \rangle$ has been explicitly shown. The data are obtained by the iDMRG calculation with the bond dimension $\chi = 600$.

is significantly suppressed in the solid state. These features are similar to that observed in the ED method [17]. Therefore, the state in the intermediate interaction region is more likely a supersolid state. This differs from the superfluid state diagnosed by the ED method, where the solidity may be underestimated by the strong finite-size effect [17]. Moreover, the visible sublattice imbalance in the structure factor revealed by the ED method, as well as the weak superfluidity, also suggests the tendency of a supersolid state. The iDMRG algorithm provides a reliable way to study the phases and phase transitions in a strongly correlated system.

The iDMRG algorithm offers great advantages to directly accessing the spontaneous symmetry-breaking state. We show, therefore, the expectation value of the boson occupancy in the upper panels of Fig. 4. The FCI state is a homogeneous state with averaged 1/4-filling on each site. Unlike the superfluid in the common partially filled bosonic system, the motion of the bosons is strongly suppressed by the presence of the flat band, resulting in the bulk insulating FCI phase in the small-V_2 region. In the intermediate region, the distribution of bosons exhibits the stripy pattern of a charge-density wave [Fig. 4(b)], in analogy to the stripy antiferromagnetism in the Heisenberg Kitaev spin model [45] and the interacting spinless fermion model on a honeycomb lattice [29]. The induced inhomogeneity weakens the band flatness, and therefore yields a weak superfluid density, in agreement with the supersolid state argued before. The stripy inhomogeneity can be continuously reduced to zero, i.e., the homogeneous state in the FCI state. Similarly, the stripy inhomogeneity can be further enhanced by introducing the sublattice imbalance, leading to the solid state at strong V_2. In this sense, the phase transition that occurred in the honeycomb lattice model is more likely a second-order transition, in accordance with the diagnosis from the characteristic quantities. Interestingly, the sublattice charge imbalance [Fig. 4(c)] in the present solid state exhibits the Knight's-move-like feature observed in the previous dipolar interacting spin system [22]. For completeness, we also show the structure factor defined as

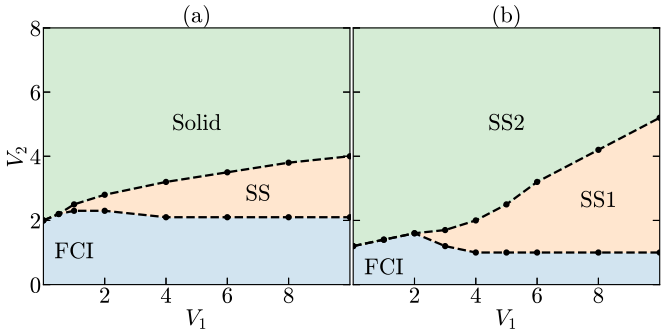

FIG. 5. V_1-V_2 phase diagrams for both (a) the honeycomb model and (b) the checkerboard lattice model. FCI and SS denote fractional Chern insulator and supersolid, respectively. The transition points used to determine phase boundaries are marked by filled circles. The iDMRG calculations are performed on an infinite cylinder of a $(2 \times 4 \times 4)$-site MPS unit cell with bond dimension $\chi = 600$.

$S(\mathbf{q}) = \frac{1}{2L_xL_y} \sum_{\mathbf{r},\mathbf{r}'} e^{i\mathbf{q}\cdot(\mathbf{r}-\mathbf{r}')}(\langle n_\mathbf{r} n_{\mathbf{r}'}\rangle - \langle n_\mathbf{r}\rangle\langle n_{\mathbf{r}'}\rangle\delta_{\mathbf{q},0})$ [46]. The resultant $S(\mathbf{q})$ (lower panels in Fig. 4) is featureless in the FCI state, peaked at (π, π) in the supersolid state, and peaked at $(\pi/2, \pi)$ (and the corresponding symmetric points) in the solid state, respectively. These features are well consistent with the density profile of the respective ground state in the thermodynamic limit. In fact, the structure factor obtained by the present iDMRG algorithm is similar to that from the previous ED results, although the superfluidity was overestimated by ED calculations [17].

The full phase diagram of the honeycomb lattice model in the V_1-V_2 space is plotted in Fig. 5(a), which shows qualitative differences from the schematic phase diagram determined by the ED method [17]. The key is that the superfluidity is much suppressed in the iDMRG calculations. Therefore, the previously diagnosed superfluid phase is substituted by the supersolid phase, as well as the much robust FCI and solid state.

B. Checkerboard lattice model

We now study the interaction-driven phase transition in the checkerboard lattice model with fixed $V_1 = 4$ using a similar iDMRG algorithm. Three distinct phases are observed according to the evolution of the above-mentioned characteristic quantities, i.e., the ground energy E_0, the entanglement entropy S, and the correlation length ξ (right panels in Fig. 2). The discontinuity of these quantities indicates that a first-order phase transition occurred at $V_2 \simeq 1$, and 2, respectively. The gapless edge modes in entanglement spectral flow and the exact $\frac{1}{2}$ unit charge pumping by a quanta flux threading demonstrate unambiguously that the weak interacting state ($V_2 < 1$) is a FCI state. The FCI state is also evidenced by the quasidegenerate sequence {1, 1, 2, 3, 5, 7} in the low-lying entanglement (Fig. 6) as discussed in the honeycomb lattice model. In contrast, the significant gap between the lowest and higher entanglement levels [Figs. 3(f) and 3(g)], together with the weak but visible sinelike oscillatory feature in the charge pumping induced by flux threading [Fig. 3(h)], indicates that the stronger interaction states ($V_2 > 1$) are more like a supersolid state (specified as supersolid-I and supersolid-II

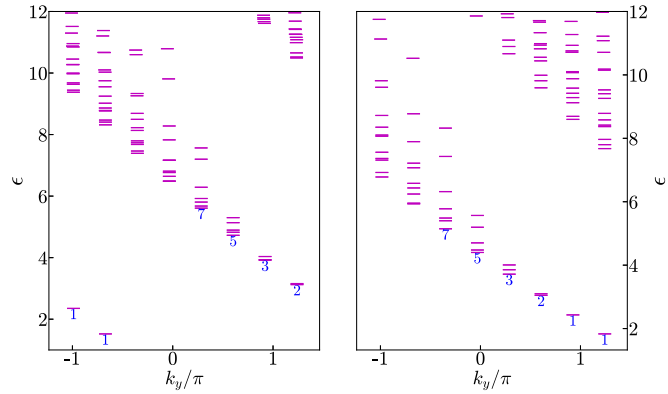

FIG. 6. Low-level entanglement spectrum in the FCI state in both the honeycomb (left panel) and the checkerboard (right panel) lattice model at $V_1 = 0$ and $V_2 = 0$. Typical counting of {1, 1, 2, 3, 5, 7} is clearly visible, consistent with chiral Luttinger liquid theory. A $(2 \times 1 \times 8)$-site MPS unit cell is adopted in iDMRG calculations with bond dimension $\chi = 800$ in both cases.

states). It should be pointed out that the oscillations in charge pumping decrease with the enhanced V_2, and they are almost negligible for $V_2 > 4$. Nevertheless, the state in the strong V_2 region remains a supersolid state since no additional phase transition is observed up to $V_2 = 8$. The reported quantum phases are similar to the previous ED diagnosis [17]. However, significant deviation can also be found. The ED predicted FCI state almost disappears and emerges in between the two supersolid states.

We further show the boson occupancy in the upper panels of Fig. 7 for a better understanding of the supersolid state. The FCI state is a homogeneous state, as expected. In comparison, the particles separate as far as possible for both sublattices and the same sublattice, in supersolid-I and supersolid-II phases, respectively. However, the boson occupancy on the sites with a minority particle remains nonzero even with strong enough

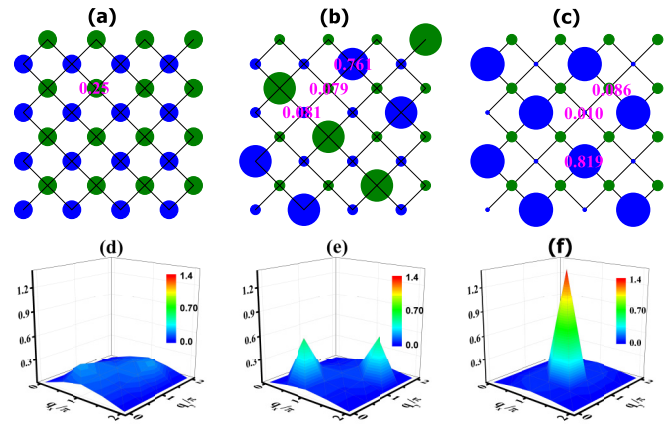

FIG. 7. Charge density profiles (upper panels) and corresponding structure factors (lower panels) of ground states in different phases in the checkerboard lattice model with fixed $V_1 = 4$. Parts (a) and (d) are for the FCI state at $V_2 = 0$ with homogeneous distributions, (b) and (e) are for the supersolid-I state at $V_2 = 1.5$, and (c) and (f) are for the supersolid-II state at $V_2 = 2.2$. Other notations are the same as in Fig. 4.

V_2, which may be the reason for the weak superfluidity. Moreover, the boson occupancy in the supersolid-I state cannot continuously transform into that in the FCI and supersolid-II state, supporting the idea of the first-order phase transition concluded based on the above-mentioned characteristic quantities. The structure factor obtained by the iDMRG algorithm (lower panels in Fig. 7) is the same as that obtained by the ED method [17], in agreement with the corresponding density profile. For completeness, we show the full phase diagram of the checkerboard lattice model in Fig. 5(b). Though the phases presented here are similar to those obtained with the ED diagnosis, the phase boundaries are quantitatively different from that in the ED results. In particular, the FCI phase emerges only in the lower V_2 region in the iDMRG diagnosis, in sharp contrast with the region $V_1 \simeq V_2$ in the ED diagnosis.

IV. SUMMARY AND DISCUSSION

In summary, we study the interaction-driven phase transition in hard-core boson systems with half-filled TFBs in two lattice models using the iDMRG algorithm. We propose an efficient way to diagnose the distinct phases by examining the entanglement spectral flows and the resultant charge pumping features with flux threading through the cylinder. The $\frac{1}{2}$-FCI state is characterized by the edge-mode-like entanglement spectral flow and a linear dependence with $\frac{1}{2}$-charge pumping on a quantum flux. We find that a robust sinelike charge pumping feature exists in the supersolid state. In comparison, the solid state features a large gap between the lowest and higher entanglement levels in spectral flow and insensitive response in charge pumping. The boson occupancy calculated by the iDMRG algorithm enables us to visualize the distinct phases. We demonstrate that phase diagrams presented here deviate significantly from those reported before by the ED algorithm, although they share similar phases, especially in the checkerboard lattice model, where qualitative differences are observed. We conclude that the iDMRG algorithm provides a reliable and convenient method to study both the topologically and conventionally ordered states.

In the iDMRG algorithm, the adopted MPS unit cell should match the translational symmetry of the represented candidate state. We try the $2 \times 2 \times 6$ MPS unit cell in both the honeycomb and the checkerboard lattice models. No qualitative difference is observed in the FCI state, the supersolid state in the honeycomb lattice model, and the supersolid-II phase in the checkerboard lattice mode, where the unit cell matches the representative ground state. This further supports our main conclusion. In addition, the supersolid and the solid state are not easy to distinguish, especially in the strong interaction region, where the superfluidity is rather weak. Calculations with larger system sizes and scaling analysis may give us a definite answer.

ACKNOWLEDGMENTS

We thank W. Zhu, T.-S. Zeng, and L.-B. Shao for helpful discussions. This work is supported by the National Natural Science Foundation of China Grant No. 11874325, and the Ministry of Science and Technology of China under Grant No. 2016YFA0300401.

[1] B. Keimer, S. A. Kivelson, M. R. Norman, S. Uchida, and J. Zaanen, From quantum matter to high-temperature superconductivity in copper oxides, Nature (London) **518**, 179 (2015).
[2] K. v. Klitzing, G. Dorda, and M. Pepper, New Method for High-Accuracy Determination of the Fine-Structure Constant Based on Quantized Hall Resistance, Phys. Rev. Lett. **45**, 494 (1980).
[3] X. G. Wen, Topological orders in rigid states, Int. J. Mod. Phys. B **04**, 239 (1990).
[4] D. J. Thouless, M. Kohmoto, M. P. Nightingale, and M. den Nijs, Quantized Hall Conductance in a Two-Dimensional Periodic Potential, Phys. Rev. Lett. **49**, 405 (1982).
[5] Q. Niu, D. J. Thouless, and Y.-S. Wu, Quantized Hall conductance as a topological invariant, Phys. Rev. B **31**, 3372 (1985).
[6] D. C. Tsui, H. L. Stormer, and A. C. Gossard, Two-Dimensional Magnetotransport in the Extreme Quantum Limit, Phys. Rev. Lett. **48**, 1559 (1982).
[7] R. B. Laughlin, Anomalous Quantum Hall Effect: An Incompressible Quantum Fluid with Fractionally Charged Excitations, Phys. Rev. Lett. **50**, 1395 (1983).
[8] F. D. M. Haldane, Model for a Quantum Hall Effect without Landau Levels: Condensed-Matter Realization of the "Parity Anomaly," Phys. Rev. Lett. **61**, 2015 (1988).
[9] G. Jotzu, M. Messer, R. Desbuquois, M. Lebrat, T. Uehlinger, D. Greif, and T. Esslinger, Experimental realization of the topological Haldane model with ultracold fermions, Nature (London) **515**, 237 (2014).
[10] E. Tang, J.-W. Mei, and X.-G. Wen, High-Temperature Fractional Quantum Hall States, Phys. Rev. Lett. **106**, 236802 (2011).
[11] T. Neupert, L. Santos, C. Chamon, and C. Mudry, Fractional Quantum Hall States at Zero Magnetic Field, Phys. Rev. Lett. **106**, 236804 (2011).
[12] K. Sun, Z. Gu, H. Katsura, and S. Das Sarma, Nearly Flatbands with Nontrivial Topology, Phys. Rev. Lett. **106**, 236803 (2011).
[13] E. J. Bergholtz and Z. Liu, Topological flat band models and fractional chern insulators, Int. J. Mod. Phys. B **27**, 1330017 (2013).
[14] S. A. Parameswaran, R. Roy, and S. L. Sondhi, Fractional quantum Hall physics in topological flat bands, C. R. Phys. Topological Insulators/Isolants Topologiques, **14**, 816 (2013).
[15] T. Neupert, C. Chamon, T. Iadecola, L. H. Santos, and C. Mudry, Fractional (Chern and topological) insulators, Phys. Scr. **2015**, 014005 (2015).
[16] D. N. Sheng, Z.-C. Gu, K. Sun, and L. Sheng, Fractional quantum Hall effect in the absence of Landau levels, Nat. Commun. **2**, 389 (2011).
[17] Y.-F. Wang, Z.-C. Gu, C.-D. Gong, and D. N. Sheng, Fractional Quantum Hall Effect of Hard-Core Bosons in Topological Flat Bands, Phys. Rev. Lett. **107**, 146803 (2011).
[18] N. Regnault and B. A. Bernevig, Fractional Chern Insulator, Phys. Rev. X **1**, 021014 (2011).

[19] Y.-F. Wang, H. Yao, Z.-C. Gu, C.-D. Gong, and D. N. Sheng, Non-Abelian Quantum Hall Effect in Topological Flat Bands, Phys. Rev. Lett. **108**, 126805 (2012).

[20] B. A. Bernevig and N. Regnault, Emergent many-body translational symmetries of Abelian and non-Abelian fractionally filled topological insulators, Phys. Rev. B **85**, 075128 (2012).

[21] Y.-L. Wu, B. A. Bernevig, and N. Regnault, Zoology of fractional Chern insulators, Phys. Rev. B **85**, 075116 (2012).

[22] N. Y. Yao, A. V. Gorshkov, C. R. Laumann, A. M. Läuchli, J. Ye, and M. D. Lukin, Realizing Fractional Chern Insulators in Dipolar Spin Systems, Phys. Rev. Lett. **110**, 185302 (2013).

[23] M. Barkeshli, N. Y. Yao, and C. R. Laumann, Continuous Preparation of a Fractional Chern Insulator, Phys. Rev. Lett. **115**, 026802 (2015).

[24] J. Motruk and F. Pollmann, Phase transitions and adiabatic preparation of a fractional Chern insulator in a boson cold-atom model, Phys. Rev. B **96**, 165107 (2017).

[25] S. Raghu, X.-L. Qi, C. Honerkamp, and S.-C. Zhang, Topological Mott Insulators, Phys. Rev. Lett. **100**, 156401 (2008).

[26] C. Weeks and M. Franz, Interaction-driven instabilities of a Dirac semimetal, Phys. Rev. B **81**, 085105 (2010).

[27] A. G. Grushin, E. V. Castro, A. Cortijo, F. de Juan, M. A. H. Vozmediano, and B. Valenzuela, Charge instabilities and topological phases in the extended Hubbard model on the honeycomb lattice with enlarged unit cell, Phys. Rev. B **87**, 085136 (2013).

[28] T. Pereg-Barnea and G. Refael, Inducing topological order in a honeycomb lattice, Phys. Rev. B **85**, 075127 (2012).

[29] S. Capponi and A. M. Läuchli, Phase diagram of interacting spinless fermions on the honeycomb lattice: A comprehensive exact diagonalization study, Phys. Rev. B **92**, 085146 (2015).

[30] J. Motruk, A. G. Grushin, F. de Juan, and F. Pollmann, Interaction-driven phases in the half-filled honeycomb lattice: An infinite density matrix renormalization group study, Phys. Rev. B **92**, 085147 (2015).

[31] H.-C. Jiang, Z. Wang, and L. Balents, Identifying topological order by entanglement entropy, Nat. Phys. **8**, 902 (2012).

[32] A. Kitaev and J. Preskill, Topological Entanglement Entropy, Phys. Rev. Lett. **96**, 110404 (2006).

[33] M. Levin and X.-G. Wen, Detecting Topological Order in a Ground State Wave Function, Phys. Rev. Lett. **96**, 110405 (2006).

[34] H. Li and F. D. M. Haldane, Entanglement Spectrum as a Generalization of Entanglement Entropy: Identification of Topological Order in Non-Abelian Fractional Quantum Hall Effect States, Phys. Rev. Lett. **101**, 010504 (2008).

[35] C. N. Varney, K. Sun, M. Rigol, and V. Galitski, Interaction effects and quantum phase transitions in topological insulators, Phys. Rev. B **82**, 115125 (2010).

[36] L. Cincio and G. Vidal, Characterizing Topological Order by Studying the Ground States on an Infinite Cylinder, Phys. Rev. Lett. **110**, 067208 (2013).

[37] Y. Zhang, T. Grover, A. Turner, M. Oshikawa, and A. Vishwanath, Quasiparticle statistics and braiding from ground-state entanglement, Phys. Rev. B **85**, 235151 (2012).

[38] A. G. Grushin, J. Motruk, M. P. Zaletel, and F. Pollmann, Characterization and stability of a fermionic $\nu = 1/3$ fractional chern insulator, Phys. Rev. B **91**, 035136 (2015).

[39] Y.-C. He, D. N. Sheng, and Y. Chen, Obtaining topological degenerate ground states by the density matrix renormalization group, Phys. Rev. B **89**, 075110 (2014).

[40] M. P. Zaletel, R. S. K. Mong, and F. Pollmann, Flux insertion, entanglement, and quantized responses, J. Stat. Mech. (2014) P10007.

[41] S.-S. Gong, W. Zhu, and D. N. Sheng, Emergent chiral spin liquid: Fractional quantum Hall effect in a kagome Heisenberg model, Sci. Rep. **4**, 6317 (2014).

[42] W. Zhu, S. S. Gong, and D. N. Sheng, Chiral and critical spin liquids in a spin-$\frac{1}{2}$ kagome antiferromagnet, Phys. Rev. B **92**, 014424 (2015).

[43] W. Zhu, S. S. Gong, and D. N. Sheng, The Z_2 and chiral spin liquids in an anisotropic kagome spin model, J. Stat. Mech. (2014) P08012.

[44] X.-G. Wen, Topological orders and edge excitations in FQH states, Adv. Phys. **44**, 405 (1995).

[45] J. Chaloupka, G. Jackeli, and G. Khaliullin, Zigzag Magnetic Order in the Iridium Oxide na_2iro_3, Phys. Rev. Lett. **110**, 097204 (2013).

[46] T.-S. Zeng and L. Yin, Fractional quantum Hall states of dipolar gases in Chern bands, Phys. Rev. B **91**, 075102 (2015).